ORNL/TM-2022/2382

Report Summarizing Progress in Digital Image Correlation Analysis of Burst Phenomenon

Nuclear Technology Research and Development

Prepared for
U.S. Department of Energy
Nuclear Technology R&D Program
Advanced Fuels Campaign

Kenneth Kane,[1] Ben Garrison[1], Samuel Bell[2], Brandon Johnston[1], Nathan Capps,[1] Kory Linton[1]

[1]Oak Ridge National Laboratory

[2]University of Tennessee, Knoxville

March 2022

M3FT-22OR020204013

ACKNOWLEDGEMENTS

This work was supported by the Advanced Fuels Campaign of the US Department of Energy Office of Nuclear Energy. The authors would like to express appreciation to Ryan Sweet and Mackenzie Ridley (Oak Ridge National Laboratory) for their technical review, and to Laurent Capolungo (Los Alamos National Laboratory) for providing technical guidance.

SUMMARY

This report is an update on the progress made towards utilizing *in-situ* methods to observe and quantify Zry-4 deformation behavior during burst testing. A heavily modified burst test was developed that allows both digital image correlation and infrared thermography to be utilized during testing to quantify strain and axial thermal gradient data during burst. A variety of tests ranging from 6.2-15.9 MPa internal pressure and utilizing both constant and transient pressure conditions were conducted and presently reported on. The test modifications, which are detailed extensively in a previous report, are effectively found to have no discernible impact on burst temperatures when compared to historical Zircaloy burst data. To support future modeling studies, the IR thermography data was used to approximate the thermal gradient down the axial length at burst for all the claddings. Then, DIC is first correlated to thermocouple temperature for a 10.3 MPa Transient pressure test, and then DIC correlated to IR thermal gradient data down the axial length of a 8.2 MPa Transient pressure test at several points.

CONTENTS

FIGURES

ACRONYMS

Loss-of-coolant accident	(LOCA)
Zircaloy-4	(Zr4)
Severe Accident Test Station	(SATS)
Oak Ridge National Laboratory	(ORNL)
Digital image correlation	(DIC)
Infrared	(IR)
Silicon carbide	(SiC)

DEVELOPMENT AND IMPLEMENTATION OF DIGITAL IMAGE CORRELATION FOR OUT-OF-CELL BURST TESTING

1. Introduction

In a previous report [1], a heavily modified burst test was developed that allowed both digital image correlation (DIC) and infrared thermography techniques to be utilized during burst to quantify the relationship between temperature, internal cladding pressure, and strain. The modifications to traditional LOCA burst testing [2–5] were as follows: (1) an air environment, (2) a 1°C/s heating rate, (3) a viewing-chamber bored through the side of the IR furnace, (4) a shortened cladding length (~76 mm), and (5) a laser-engraved DIC pattern. Based off the few data points collected previously, it was unclear if these modifications altered the test in such a way as to limit the relevance of the data collected. Therefore, in the following report, a more extensive test matrix was conducted at a variety of internal cladding pressures and under both constant and transient pressure conditions (pertaining to running an open or closed valve test, respectively). The expanded test matrix is not solely to evaluate the impact of modifications, but more widely intended to generate *in-situ* data to compare to modeling and simulation of the burst event. Ultimately, the envisioned goal is to generate better data to inform high fidelity performance fuel codes, like BISON, that will provide avenues towards accelerated fuel qualification.

The expanded test matrix has been completed and will be reported on in the following text. A fully analyzed test consists of the calculation of hoop, axial, and radial strain and the axial thermal gradient data down the length of the cladding, where both the strain and thermal gradient data are correlated together throughout the entire test. Full analysis is on-going but is updated presently. The modified burst test is briefly described, and the burst temperatures and pressures of the expanded test matrix is also reported. For each test, the axial thermal gradient at burst was analyzed, with the goal of implementing the observed thermal gradients into BISON to simulate the burst. For one test, the axial thermal gradient during the entire burst test was analyzed, where cladding emissivity had to be constantly adjusted to match an "anchoring" thermocouple. For correlating strain with temperature, there are two techniques, one previously established [1] where strain is correlated with thermocouple reading, and one presently implemented where strain is correlated down the axial length at several points with the IR thermal gradient data during the entire burst test.

2. Summary of Experimental Design

A photograph of a Zry-4 cladding train assembly situated inside the 8-kW IR furnace is shown in Figure 1(a). The nominal pre-transient geometry of the Zry-4 segment was 9.5 mm outer diameter, 0.575 mm wall thickness, and 76 mm length (the shortened length will be discussed below). To simultaneously collect light optical and IR thermography images during testing, several key modifications to traditional LOCA burst testing [3,4] were necessary. The modifications are discussed in greater detail in a prior report [1], but will be briefly discussed in the following. First, to observe cladding deformation a ~38 mm ID through-hole was bored through the side of the furnace body. A direct line-of-sight photograph of the cladding through the viewing chamber at room temperature is shown in Figure 1(b). Second, in order to ensure cladding deformation was visible, a shortened ~ 76 mm length of cladding had to be used, with thick-walled 316SS extension tubing to center the cladding directly in front of the viewing chamber. Third, the test had to be conducted in air rather than steam due to the quartz reaction tube itself beginning to emit IR radiation upon reaching higher temperatures, rendering the cladding no longer visible in the IR. Fourth, a SiC "C" shell was machined from Hexoloy SA SiC to prevent direct reflection of the IR lamps off the cladding surface. This is schematically illustrated in Figure 1(c). Due to Zry-4 being a graybody rather than a perfect

blackbody, a certain fraction of incident IR is reflected off the surface. When observing the Zry-4 cladding during burst test without the SiC "C" shell, the Zry-4 surface temperature cannot be accurately calculated due to the direct IR reflection from the IR lamps. The SiC shell, being much closer to a blackbody, absorbs most incident IR and in turn acted as a heating element in proximity with the cladding. There will be heat transferred from the upper and lower portions of the cladding train assembly that were still directly irradiated by the furnace. To control and monitor temperature during testing, two thermocouples were placed on the cladding train assembly, shown in Figure 1(a): a control thermocouple ($T_{control}$) and a sample thermocouple (T_{sample}), herein referred to as T_{front}. The heating profile (which will be shown in the results section) was controlled via $T_{control}$. When $T_{control}$ was placed inside the shell, the indirect heating was insufficient to maintain a controlled heating profile. Thus, $T_{control}$ was situated immediately outside the SiC shell, visible to direct IR heating. T_{front} was situated immediately below the top compression fitting and bent in a manner to maintain surface contact during burst. After conducting several burst tests, the burst opening would sometimes occur on the backside of the cladding. An additional thermocouple was placed on the backside of the cladding (T_{back}, not shown) to monitor temperature. The entire cladding train assembly is fixed at both ends of the furnace.

The fifth and final modification was the DIC pattern for calculating strain as a function of time and temperature. The pattern consisted of squares drawn with a BOQX laser-engraver and has been used previously for both *in-situ* [6] and before/after [7] burst strains measurements. An image taken at a time t_1 during a burst test where deformation begins to be visible is shown in **Error! Reference source not found.**(a), and another later at t_2 immediately prior to burst is shown in **Error! Reference source not found.**(b). A higher magnification image at t_2 showing the DIC pattern is reported in **Error! Reference source not found.**(c). Structured light scans with a Keyence 3100 determined these squares to be ~ 14 µm in depth. The individual DIC objects collectively served as the back drop for node identification and tracking during DIC calculation.

A GT6600 camera was used to collect DIC images and a FLIR E95 camera was used to collect IR images during burst test. To mitigate parallax error, a TC16M120 telecentric lens was attached to the digital camera. In an earlier report [1] a series of IR/visible mirrors and lens were used to split the visible and IR light coming from the viewing chamber, but due to significant IR resolution loss, this experimental set up was discarded. Instead, a visible light mirror was placed at a 45°C angle in front of the viewing chamber, with an additional IR mirror (Edmund Optics, Part # 64470) placed in front of the telecentric lens to reduce light intensity (visible transmission coefficient ~ 85%). The IR camera was then able to be placed at ~ 1 m from the cladding at a slight angle, allowing a direct line-of-sight view past the visible light mirror.

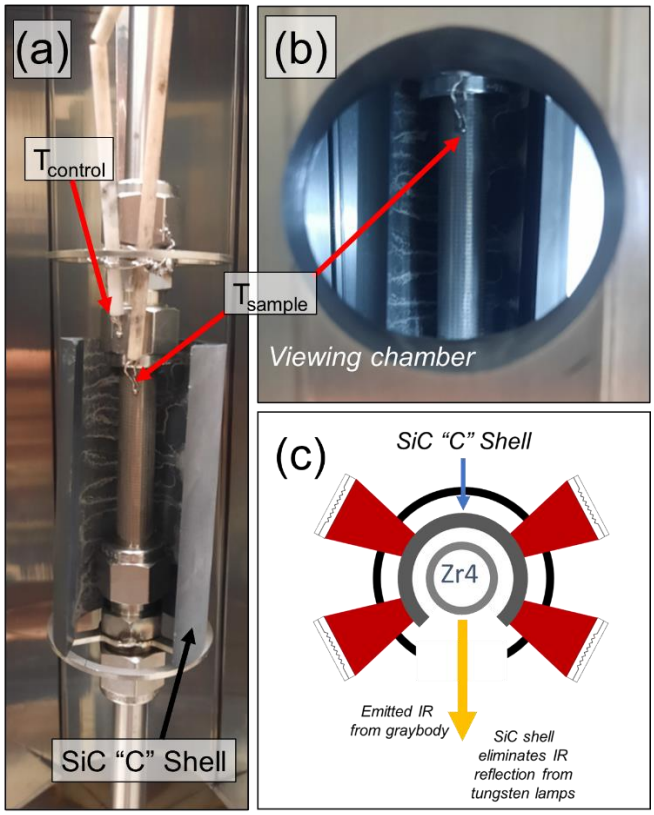

Figure 1 (a) Photograph of the shortened cladding train assembly inside the IR furnace with locations of control and sample thermocouples. (b) Line-of-sight photograph through the viewing chamber bored through the side of the IR furnace. (c) Graphical illustration of the SiC "C" shell blocking direct IR irradiation of the cladding.

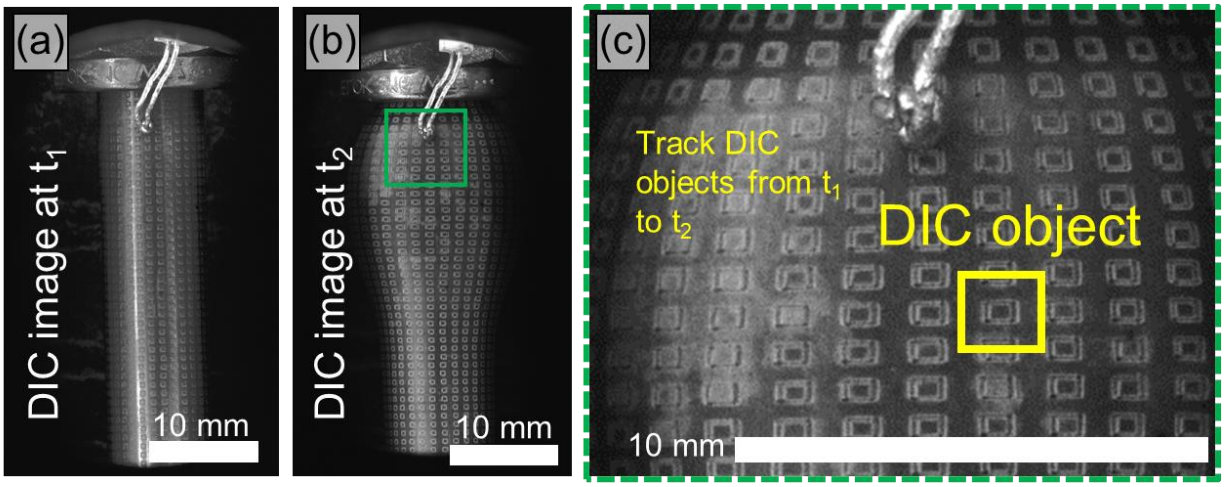

Figure 2 Images from the DIC camera taken at (a) a time t_1 when visible deformation begins and (b) later at time t_2 immediately prior to burst. (c) Higher magnification image at t_2 s showing the laser-engraved box pattern utilized for calculating strain rates as a function of time

3. Results

3.1 Test matrix, burst pressures, and burst openings

As outlined in the introduction, DIC burst tests were conducted at variety of nominal initial cladding pressures under both constant pressure and transient pressure conditions, where a constant pressure test was performed by leaving the pressure valve open and the transient pressure test was performed by closing the valve. The constant pressure tests more closely emulate traditional creep testing while the transient pressure tests are representative of LOCA conditions. The testing conditions, burst temperatures, burst pressures, and other test specific data are reported in Table 1. For all tests, burst hoop stress was calculated based on the pre-transient cladding geometry utilizing a thin-walled approximation.

The first test conducted was 8.2 MPa Transient and the burst opening occurred on the back side of the cladding. For all subsequent tests, an additional thermocouple was placed on the backside of the cladding to monitor temperature, hence all tests other than 8.2 MPa Transient report the temperatures of a control, front, and back thermocouple. For claddings that burst on the back, T_{back} was taken as the burst temperature. For the ~15.9 MPa Transient test, the cladding had to be relieved of pressure during the 300°C hold as there were concerns the cladding pressure would climb above the upper limit of the pressure transducer, 3000 psi (20.67 MPa).

Table 1 Test conditions and results

Nominal initial pressure (MPa)	Nominal pressure condition	Burst pressure (MPa)	Burst hoop stress (MPa)	$T_{control}$ (°C)	T_{front} (°C)	T_{back} (°C)	Burst location	Compression fitting displacement?
6.2	Constant	6.01	47	763	797	833	Back	Yes
6.2	Transient	7.63	59	758	738	777	Back	No
8.2	Constant	8.18	63	756	744	768	Back	Yes
8.2	Transient	10.36	80	736	682	NA	Back	No
10.3	Constant	10.11	78	747	687	721	Back	Yes
10.3	Transient	12.92	100	697	656	680	Between	No
15.9	Constant	14.99	116	670	671	617	Front	No
~15.9	Transient	15.61	121	653	630	680	Front	No

As seen in the last column of Table 1, there was a tendency for the top compression fitting to slightly displace during the temperature ramp, presumably due to the shortened cladding length (~76 mm) causing the compression fittings to reside much closer to the middle zone of the furnace (the "hottest" region). It's possible that at these more elevated temperatures, the compression fittings are not as secure. Regardless, the displacement was not enough to result in complete pressure loss but did result in sudden and temporally localized perturbations in temperature and pressure readings because (1) the displacements caused a small increase in volume and (2) the thermocouples are secured via Pt-Rh wire to the top compression fitting. This phenomenon is shown in Figure 3. The temperature and pressure profiles during the 6.2 MPa Transient pressure DIC burst test is reported in Figure 3(a) and in closer proximity to the burst event in Figure 3(b). Due to the SiC "C" shell, a temperature gradient develops between $T_{control}$, which resides outside the shell, and both T_{front} and T_{back}, which reside inside the shell. A similar series of temperature and pressure profiles during the 6.2 MPa Constant pressure test are shown in Figure 3(c)- Figure 3(d). In Figure 3(c), the perturbance in pressure and temperature readings is clearly seen at ~1200 s, where internal cladding pressure slightly drops and then normalizes to the pressurizing gas cylinder and temperatures suddenly drop, rapidly increase, then settle back to a ~ 1°C/s heating rate. In total, the perturbation event lasts approximately 30 seconds. The actual cladding temperature is assumed to continue to increase at 1°C/s through the event, as evidenced by the normalization of all three temperatures after the perturbation.

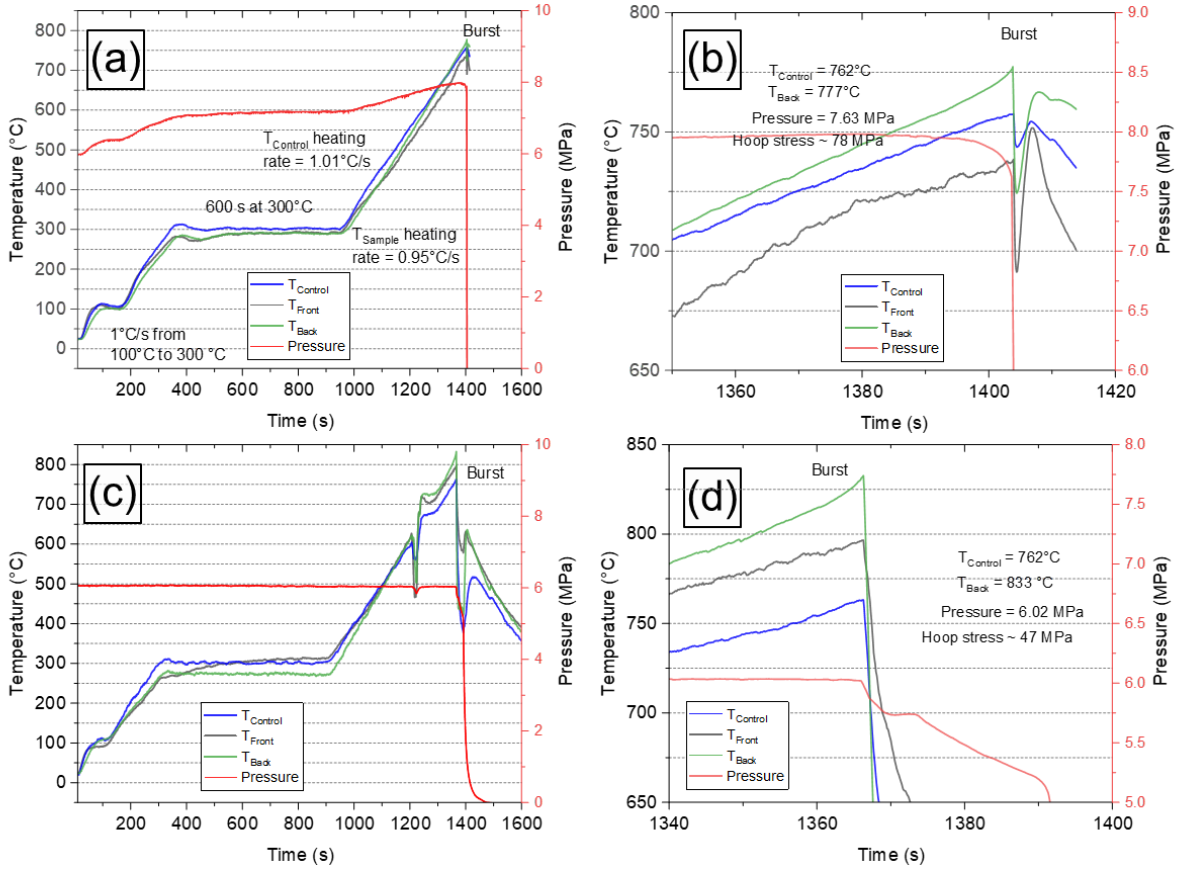

Figure 3 Temperature and pressure profiles for the (a,b) 6.2 MPa Transient and (c,d,) 6.2 MPa Constant pressure tests showing the impact compression fitting displacement has on measured pressures and temperatures

The relationship between the burst temperatures and pressures of Table 1 are plotted in Figure 4. For claddings that burst on the back-side, the burst temperature is T_{back} (black), while for those that burst in the front or side, T_{front} is the burst temperature (red). Constant pressure tests are marked as stars, while transient pressure tests are marked as squares. There was no apparent difference in burst temperature behavior between constant or transient pressure tests. The Chapman correlation [8,9] for Zircaloys heated at 1°C/s is included as historical reference. At temperatures above 700°C. there was good agreement with the Chapman correlation. At temperatures < 700°C, burst pressures were slightly higher but consistent with Sawarn *et al.* [10], who also reported a deviation from the correlation at lower temperatures. The Chapman correlation was calculated based on test programs that only burst claddings above 700°C, where Zircaloys will be, depending on temperature, either in a mixed α + ß or single ß-phase region. Below 700°C, the cladding may be in the single α-phase region. Future studies will incorporate detailed microstructural analysis of the claddings prior to the DIC burst test to verify phase microstructure.

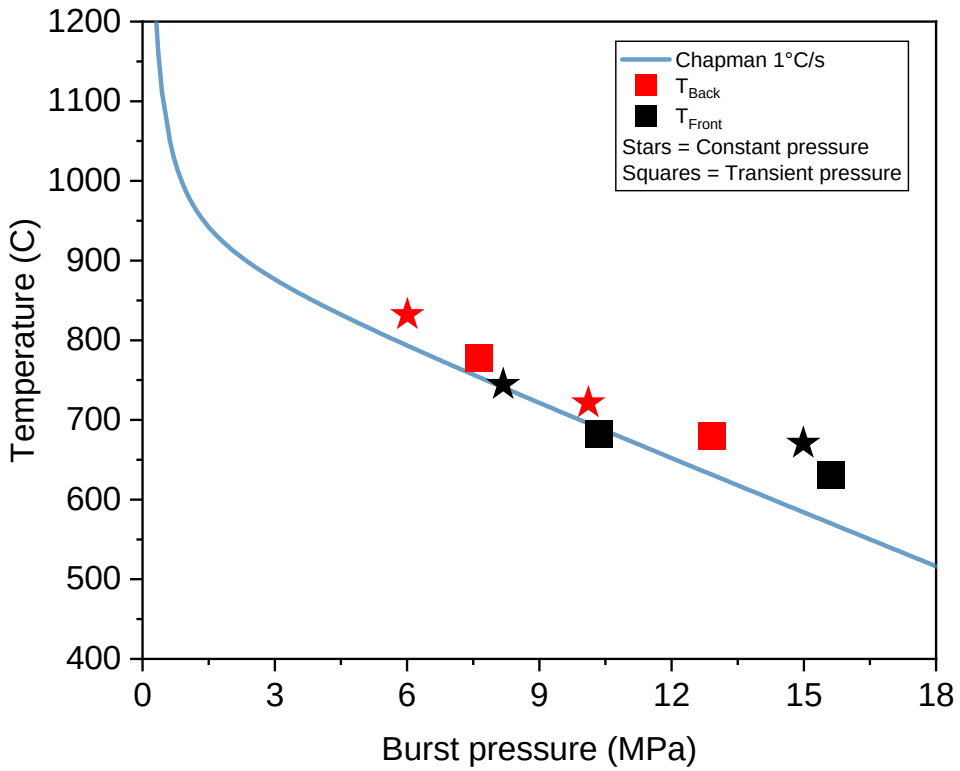

Figure 4 Relationship between burst temperatures and burst pressures of Zry-4 segments subjected to the DIC burst test.

Optical macrographs of all the claddings after burst testing are shown in Figure 5. Burst openings always formed in the vicinity of the top compression fitting. Experimentation was conducted to try and instigate the opening closer to axial center but were unsuccessful, presumably due to the combination of the viewing chamber and the shell always resulting in the top compression vicinity being the hottest segment of the cladding. Additionally, openings appeared to propagate down the axial "center" of a laser-engraved box column, indicating the laser-engraving may impact crack initiation and propagation. But as can be seen in Figure 4, there is no noticeable impact on burst temperatures.

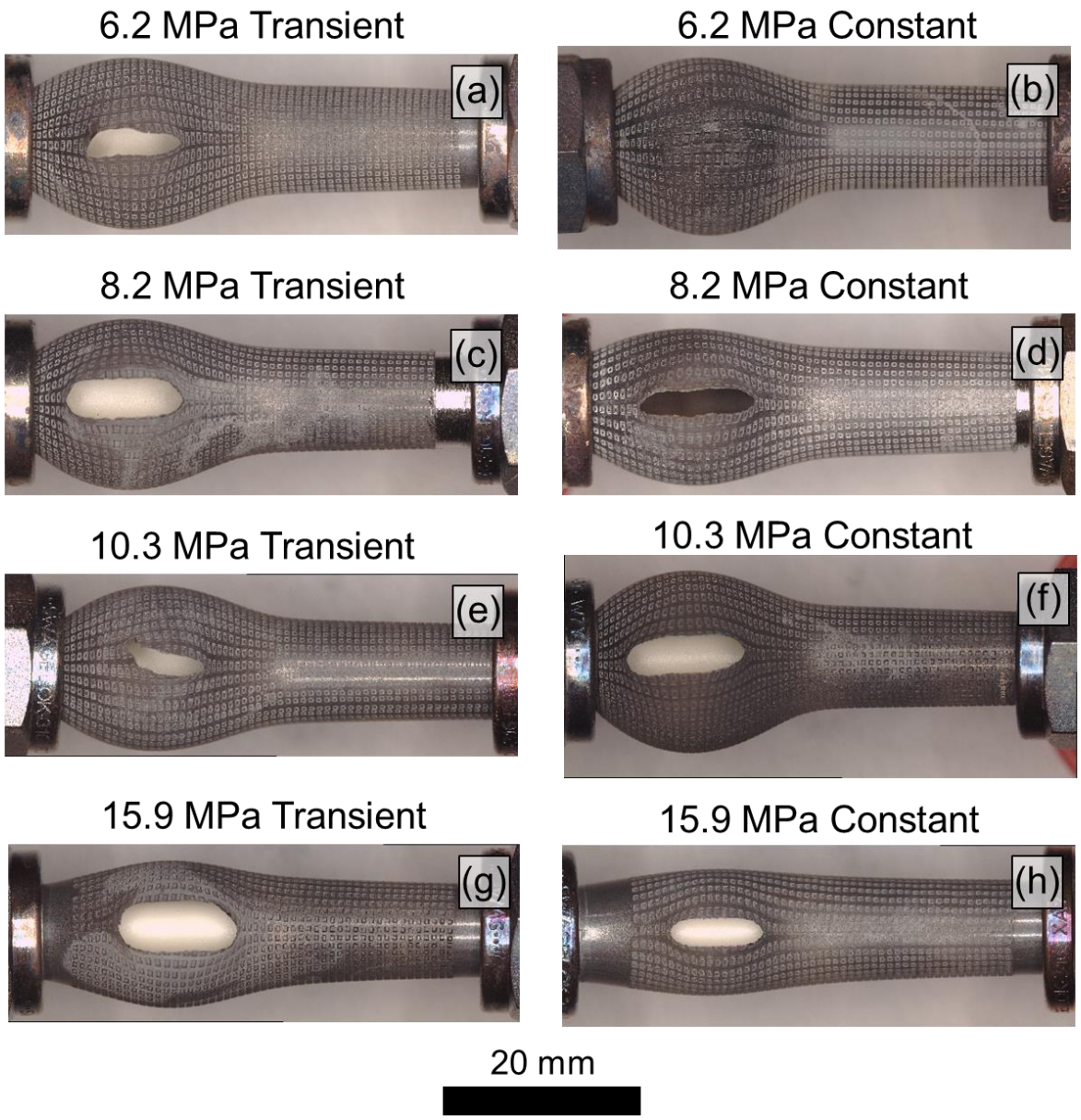

Figure 5 Optical macrographs of (a) 6.2 MPa Transient, (b) 6.2 MPa Constant, (c) 8.2 MPa Transient, (d) 8.2 MPa Constant, (e) 10.3 MPa Transient, (f) 10.3 MPa Constant, (g) 15.9 MPa Transient, and (h) 15.9 MPa Constant claddings after burst.

3.2 Thermal gradient at burst

The IR data was used to approximate the axial thermal gradient at burst. Similar to other groups studying the burst behavior of Zr-based nuclear alloys [11], there was a discrepancy between emissivity values reported in the literature and the emissivity values necessary to align IR readings to thermocouple readings. The difficulties of IR thermography during transient temperature testing has been detailed to a greater extent

in a previous report [1]. Due to the discrepancies and the approximate nature of the readings, it was necessary to always conduct the burst test with T_{front} in view. An optical macrograph of the 6.2 MPa Constant cladding immediately prior to burst is shown in Figure 6(a), and the IR thermal map taken at the same approximate instant is shown in Figure 6(b). To estimate the gradient at burst, a line profile was drawn down the axial center of the cladding immediately prior to burst, and emissivity adjusted so that the IR reading in the vicinity of T_{front} matches the thermocouple reading.

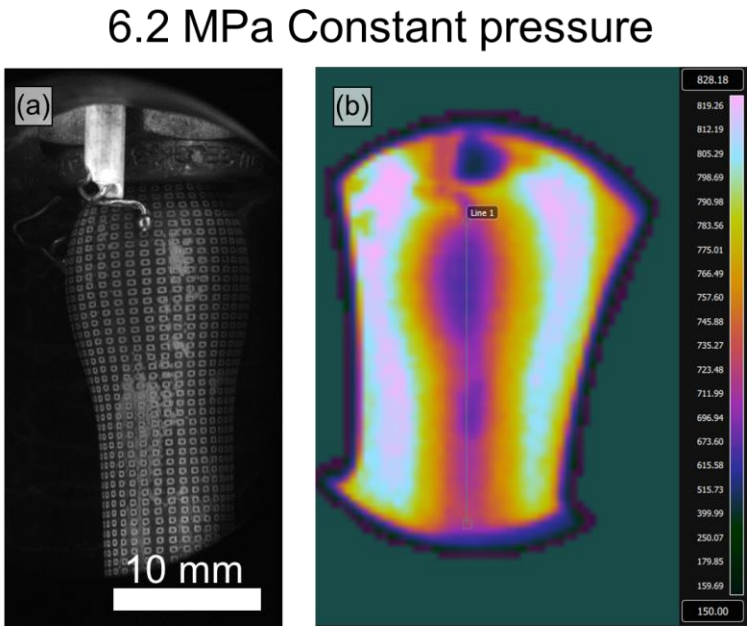

Figure 6 (a) Optical macrograph and (b) IR thermal map of the 6.2 MPa Constant pressure cladding immediately prior to burst. The direction of a thermal line profile is drawn in (b)

The calculated thermal gradients down the axial lengths calculated in the above-described manner are reported in Figure 7. For some tests, there was a tendency for the IR temperature to spike towards the center of the line profile. This spike generally corresponds to the bottom of the ballooning region (seen approximately midway of the line profile drawn in Figure 6. At immediate glance, there is no clear relationship amongst the tests, as for some the temperature begins to rise midway down the axial length, and for other tests the temperature continues to decrease. This discrepancy in behavior may be due to poor resolution of the IR camera. Regardless, it may be possible to generalize the gradient as a function of temperature to apply to all cases.

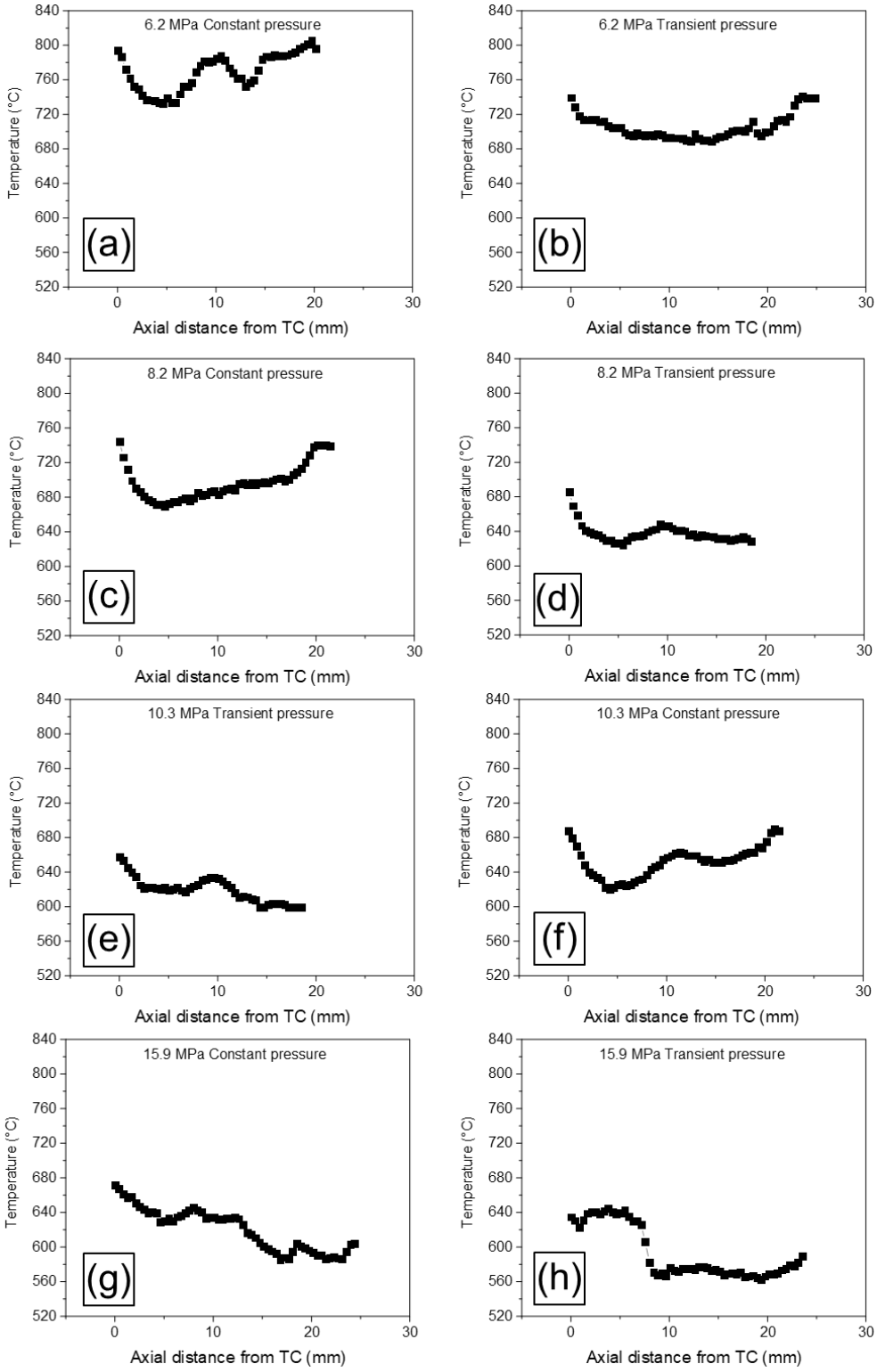

Figure 7 Thermal gradients down the axial cladding length immediately prior to burst for (a) 6.2 MPa Transient, (b) 6.2 MPa Constant, (c) 8.2 MPa Transient, (d) 8.2 MPa Constant, (e) 10.3 MPa Transient, (f) 10.3 MPa Constant, (g) 15.9 MPa Transient, and (h) 15.9 MPa Constant pressure.

By continuously adjusting emissivity to match T_{front}, it was possible to estimate the thermal gradient as a function of time during the entire DIC burst test. An IR thermal image immediately prior to burst of the 8.2 MPa transient pressure test is shown in Figure 8(a), and the axial thermal gradient as a function of time in Figure 8(b). The thermal gradient immediately prior to burst is shown in Figure 8(c) and the average cladding temperature as a function of time in Figure 8(d). Although no generalized thermal gradient behavior could be deduced immediately from the gradients at burst (Figure 7), determination of the axial thermal gradients during the transient heating from all tests may reveal a standard gradient profile. For instance, the highest burst temperature was achieved by the 6.2 MPa Constant pressure test (833°C), and the axial thermal gradient during this test may reveal a general gradient profile that could be applied to all tests.

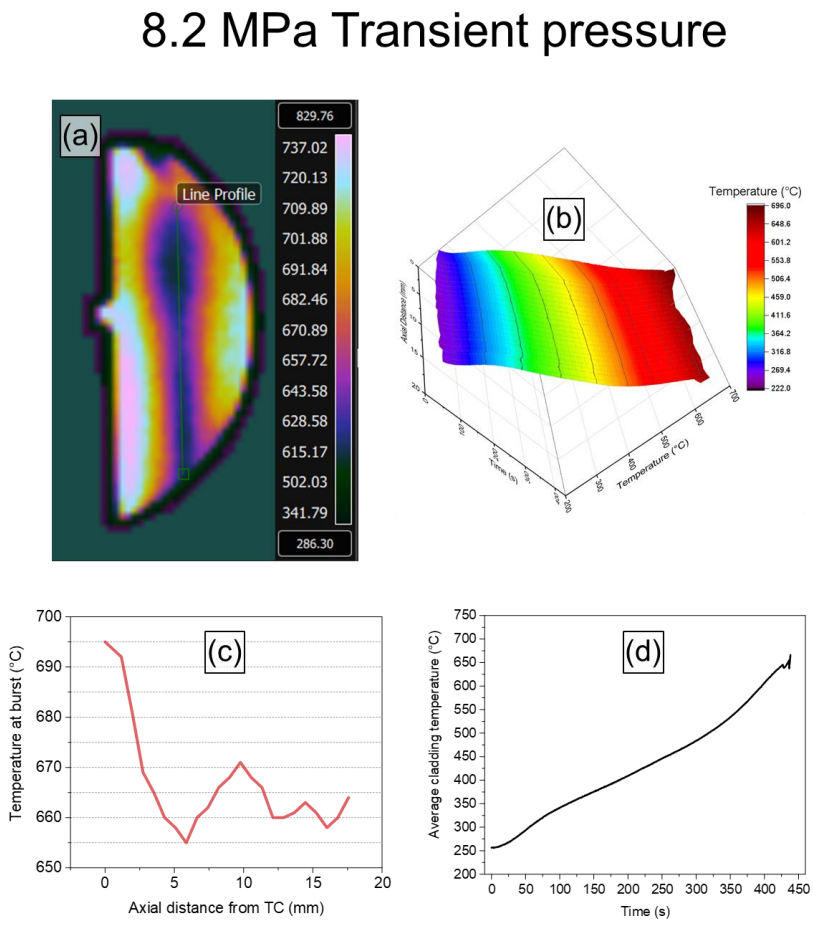

Figure 8 (a) IR thermal image immediately prior to burst of the 8.2 MPa Transient pressure test and (b) the thermal gradient down the axial length as a function of time. (c) The thermal gradient down the axial length at burst and (d) the average cladding temperature as a function of time

4. Quantifying the relationship between temperature, internal cladding pressure, and deformation

The DIC technique is performed on the front side of the cladding where T_{front} is used to correlate strain to thermocouple temperature even if burst occurred on the back side. In a prior report [1], the 8.2 MPa Transient pressure test was analyzed utilizing DIC in conjunction with the front cladding temperature. In an identical manner, the 10.3 MPa Transient pressure test was analyzed in a region in the vicinity of the sample thermocouple and the strain data is reported in Figure 9. Analysis is on-going to complete the DIC calculations of the other tests.

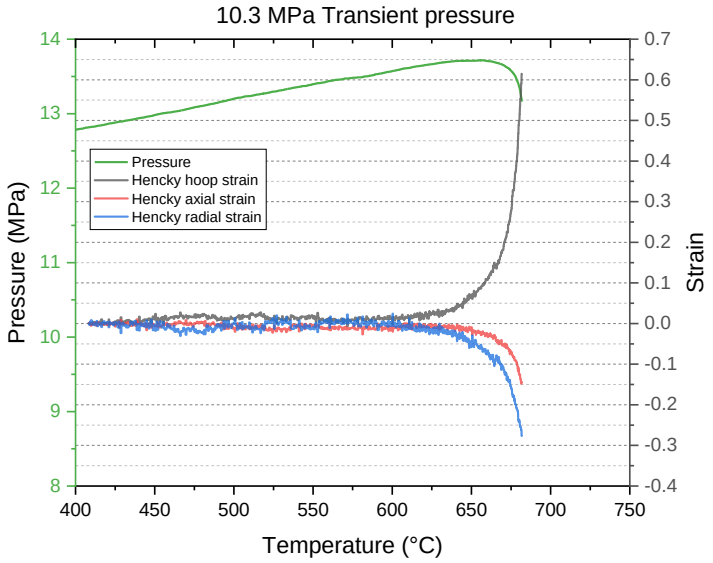

Figure 9 The relationship between temperature (T_{front}), internal cladding pressure, and strain during a DIC burst test under 10.3 MPa transient pressure conditions

Rather than correlate the DIC strain data to thermocouple temperature, it's possible to correlate strain and temperature down the cladding axial length utilizing the thermal gradient profile shown in Figure 8(b). For the 8.2 MPa Transient pressure test, DIC was performed at 5 different points down the cladding axial length, and the calculated strains were correlated with the thermal gradient data. A light optical macrograph of the 8.2 MPa Transient pressure test cladding immediately prior to burst is shown in Figure 10 and the hoop and axial strains during testing at five different points down the axial length. The internal cladding pressure is included for Point #1 however this is only an approximation, as the relationship between cladding pressure and temperature is only known for the thermocouple temperatures (pressure and thermocouple temperature are monitored via LabView). Thus, correlating internal cladding pressure and IR temperature will yield different pressure profiles for every point down the axial length in Figure 10. When comparing strain data down the axial length, correlating to time rather than temperature will allow correlation with internal cladding pressure.

Radial strain is not measured directly but is calculated from the hoop and axial strains assuming conservation of volume. When utilizing the IR thermal data to correlate the strain, there is a larger degree of data spread in the few seconds leading up to burst due to the point-to-point noise in the IR thermal data. To eliminate this, a smoothing function could be utilized for the IR thermal gradient data and will be implemented in future studies, but as mentioned above, temporal comparisons may be more informative.

Points #2 and #3 were intentionally taken in close proximity to evaluate reproductivity of the strain calculations. As can be seen, both the hoop and axial strains at #2 and #3 are nearly indistinguishable from each other. Comparing the top three points to #4 and #5, hoop and axial strains decrease in magnitude down the axial length, as expected based on the visual deformation behavior.

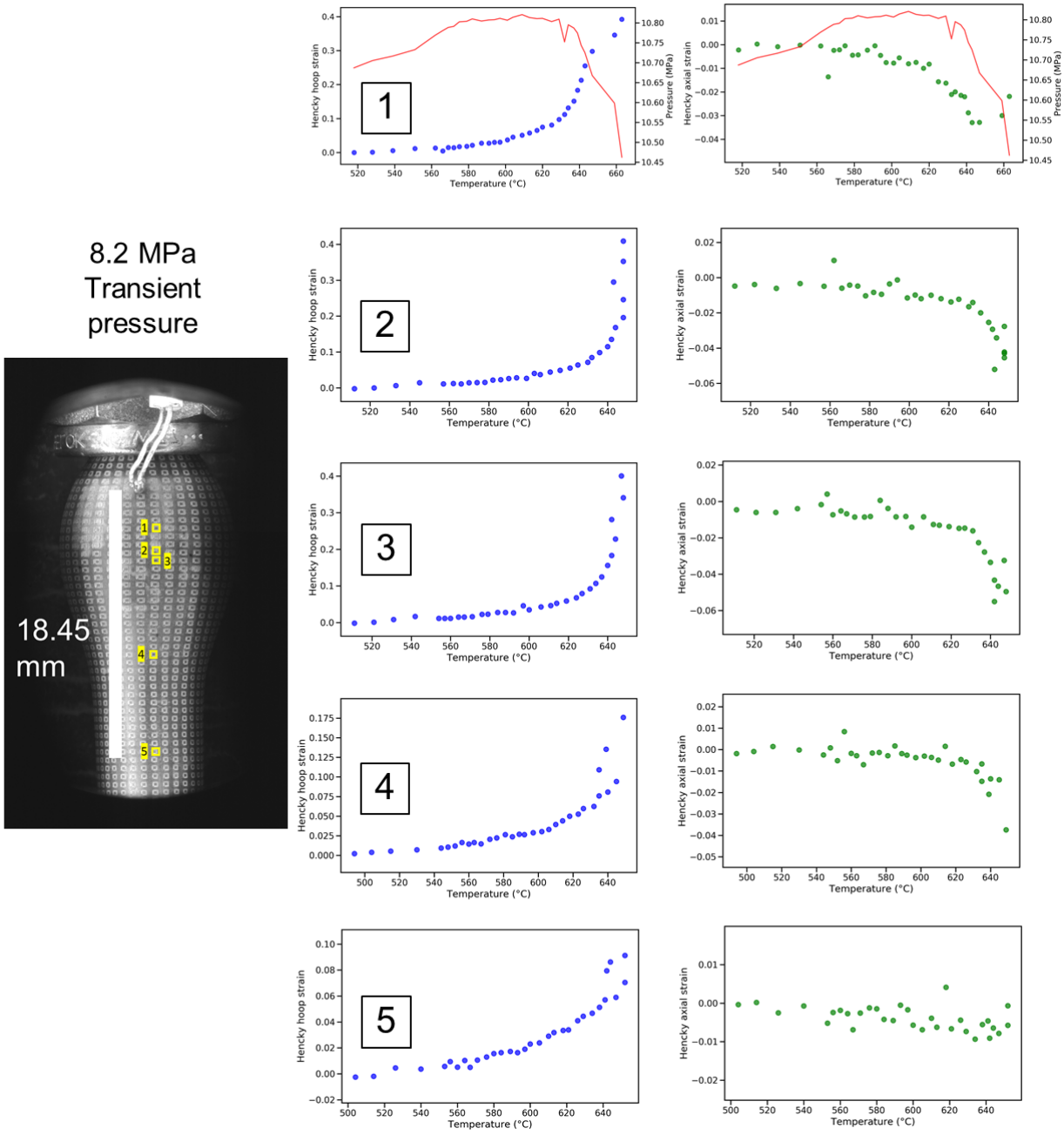

Figure 10 The 8.2 Transient pressure test and the hoop and axial strains at five different points down the axial length, with strain correlated to the IR thermal gradient data. The cladding internal pressure is shown in red for the strain data taken from point 1.

5. Summary and Conclusions

An expanded DIC burst test matrix was conducted at pressures of 6.2 – 15.9 MPa under both constant and transient pressure conditions. Burst temperatures and pressures are in agreement with historical data, indicating the heavily modified DIC burst does not appreciably influence burst temperatures compared to traditional LOCA burst testing. IR thermography was utilized to quantify axial thermal gradients immediately prior to burst for the entire test matrix and for one pressure condition, the evolution of the gradient during the entire burst test. The thermal gradient as a function of time and location was then correlated with strain measurements calculated down the axial length of the cladding. The resultant strain rates down the axial length were reproducible when adjacent nodes were used and were consistent with the differences in visible deformation.

6. References

[1] K. Kane, N. Capps, B. Garrison, B. Johnston, S. Bell, K. Linton, Development and Implementation of Digital Image Correlation for Out-of-Cell Burst Testing, Oak Ridge National Lab.(ORNL), Oak Ridge, TN (United States), 2021.

[2] B. Garrison, K. Linton, K. Kane, S. Bell, T. Graening, C.S. Hawkins, B. Johnston, A.T. Nelson, AFC Burst Activities with Coated Zircaloy4 Under Accident Conditions, 2021.

[3] S.B. Bell, K.A. Kane, C.P. Massey, L.A. Baldesberger, D. Lutz, B.A. Pint, Strength and rupture geometry of un-irradiated C26M FeCrAl under LOCA burst testing conditions, J. Nucl. Mater. 557 (2021) 153242. doi:10.1016/j.jnucmat.2021.153242.

[4] C.P. Massey, K.A. Terrani, S.N. Dryepondt, B.A. Pint, Cladding burst behavior of Fe-based alloys under LOCA, J. Nucl. Mater. 470 (2016) 128–138. doi:10.1016/j.jnucmat.2015.12.018.

[5] S.B. Bell, T. Graening, A. Evans, P. Kelly, B.A. Pint, K.A. Kane, Burst and oxidation behavior of Cr-coated Zirlo during simulated LOCA testing, J. Nucl. Mater. (2022) 153679.

[6] M.N. Gussev, M. Howell, K. Terrani, A. Nelson, Execution of Targeted Experiments to Inform BISON for ATF Materials: An Advanced Approach to Tube Burst Testing, Oak Ridge National Lab.(ORNL), Oak Ridge, TN (United States), 2019.

[7] B. Garrison, M.N. Cinbiz, M. Gussev, K. Linton, Burst characteristics of advanced accident-tolerant FeCrAl cladding under temperature transient testing, J. Nucl. Mater. 560 (2022) 153488. doi:10.1016/j.jnucmat.2021.153488.

[8] R.H. Chapman, Multirod burst test program, Department of Energy,[Office of Energy Technology], Oak Ridge National …, 1978.

[9] D.A. Powers, R.O. Meyer, Cladding swelling and rupture models for LOCA analysis. Technical report, Nuclear Regulatory Commission, 1980.

[10] T.K. Sawarn, S. Banerjee, K.M. Pandit, S. Anantharaman, Study of clad ballooning and rupture behavior of fuel pins of Indian PHWR under simulated LOCA condition, Nucl. Eng. Des. 280 (2014) 501–510. doi:10.1016/j.nucengdes.2014.10.011.

[11] R. Nagy, M. Király, P. Petrik, Z. Hózer, Infrared observation of ballooning and burst of nuclear fuel cladding tubes, Nucl. Eng. Des. 371 (2020). doi:10.1016/j.nucengdes.2020.110942.